Design of PMSM for EMA Employed in Secondary Flight Control Systems

P. Giangrande[1], A. Al-Timimy[1], A. Galassini[1], S. Papadopoulos[1], M. Degano[1,2], M. Galea[1,2]

[1] Power Electronics, Machines and Control Group, University of Nottingham, Nottingham, UK, p.giangrande@nottingham.ac.uk

[2] School of Aerospace, University of Nottingham Ningbo, Ningbo, China

***Abstract* — The more electric aircraft (MEA) initiative aims to improve weight, fuel consumption and maintenance costs of the aircraft, by increasing the use of electric power in actuation systems. Considering this scenario, electromechanical actuators (EMAs) for flight control (FC) systems represent a key technology in future aircraft. The paper presents a linear geared EMA for secondary FC systems, where the safety and availability requirements are fulfilled by duplicating the electric drive acting on the EMA drive-train (i.e. two power converters feeding as many electrical machines coupled to the same mechanical system). The design of the permanent magnet synchronous machine (PMSM) integrated into the EMA is addressed. Preliminary results on the PMSM prototype are also provided and compared to the finite element (FE) outcomes obtained at the design stage. The EMA performance at system-level is evaluated in Dymola environment, analyzing three operating modes, such as active-active, active-standby and active-shorted. Finally, some thermal considerations regarding the active-shorted configuration are outlined.**

Keywords—EMA, EHAs, Secondary Flight Control Surfaces, PMSM, Fault-Tolerant Architecture, Dymola.

I. INTRODUCTION

In recent years, demanding regulations on fuel emissions and the need of decreasing both operating and maintenance costs have encouraged the aircraft industry to move from conventional hydraulic to electrical actuation systems [1-3]. Such trend is supported by the inherent benefits offered by electrical actuation systems, like: a) weight reduction due to the removal of hydraulic pipelines, b) high dynamic performance ensured by both low inertia motors and high-bandwidth controllers and c) actuation distribution degree of freedom [4].

Among the electrical actuation solutions, mainly two configurations can be identified: electro-hydrostatic actuators (EHAs) [5] and EMAs [6, 7]. In the former, electric power is used for suppling the electric drive, which is mechanically coupled to a hydraulic pump. Hence, hydraulic power is locally generated for driving the FC surface. On the other hand, a mechanical drive-train (e.g. gearbox and/or ball screw) is placed between the electric drive and the FC surface [8], as schematically shown in Fig. 1. Both EHAs and EMAs are currently employed on large commercial aircraft. In particular, Boeing 787 uses EMAs for landing gear braking and spoiler surface [9]. Similarly, the counterpart Airbus A380 adopts EHAs for ailerons and elevators (i.e. primary FCs), while slats (i.e. secondary FCs) are actuated by EMAs [10]. The adoption of EHAs for the primary FCs led to a 1500 kg weight reduction on Airbus A380 [11]. Despite the local hydraulics (i.e. internal reservoir) and the higher maintenance costs (i.e. oil leak and/or disposal), at the moment, the mixed solution represented by the EHAs is more widespread than EMAs, due to the well-established "know-how" regarding hydraulic systems [11]. Indeed, the risk of failures (e.g. jamming) and the lack of accumulated reliability experience relegate EMAs to be currently implemented on secondary FCs, such as flaps, spoilers and slats [9]. These FC surfaces are considered less safety-critical, due to the inherent surface redundancy of the aircraft wing, which is equipped with multiple FC surfaces performing the same aerodynamic task [12]. Nevertheless, EMAs represent an attractive technology, which is gaining interest due to its higher efficiency and further weight reduction compared to EHAs [1, 3].

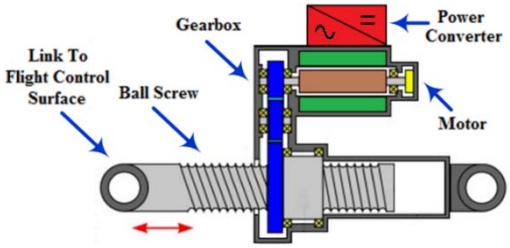

Fig. 1. Example of linear geared EMA.

A linear geared EMA for secondary FC systems is considered in this work. Despite the surface redundancy of the aircraft wing, the EMA availability has been increased by duplicating the electric drive. Hence, two electrical machines powered by separate power electronics converters (PECs) are used for driving the EMA drive-train, as sketched in Fig. 2.

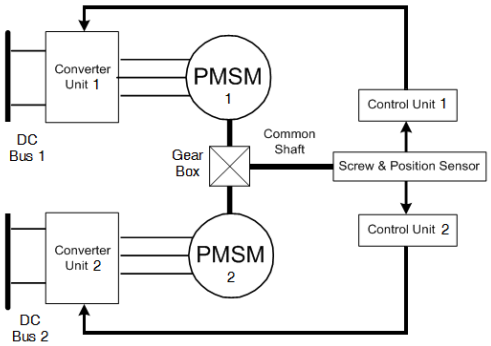

Fig. 2. Architecture of the EMA under analysis.

This architecture allows to achieve the safety requirements in case of a fault occurring in the electric drive components (i.e. PECs and motors), which have higher failure rate. In order to meet the challenging volume requirement, PMSM is selected as machine topology, due to its high-power density [13-15]. The PMSM performance is discussed along with some design/manufacturing details (e.g. rotor retaining sleeve, permanent magnet segmentation and hollow shaft). The preliminary PMSM prototype results are presented and

compared against the ones obtained at the design stage via FE analysis. Since the EMA drive-train (i.e. gearbox plus ball screw) is not yet available for integration tests, the EMA performance is simulated in Dymola environment, using purpose built models for the electric drive components [16]. In particular, the three EMA operating modes, such as active-active, active-standby and active-shorted [12], are investigated. Due to the high current flowing through windings during the active-shorted configuration, the PMSM hot-spot temperature has been predicted by using a lumped parameter thermal network (LPTN) built according to [17].

II. PMSM Design and Considerations

Considering the application under study, the PMSM is required to deliver 5 Nm at 8000 rpm and operate at a maximum ambient temperature of 70 °C using natural air cooling system. Furthermore, to comply with the fast-dynamic response requirements, the moment of inertia should not exceed 10^{-4} kg·m^2. According to these specifications and taking into account the limited available space (i.e. axial length ≤ 80 mm and outer diameter ≤ 80 mm), the design has been performed via FE analysis. A preliminary trade-off study has been carried out for selecting the appropriate slots/poles combination. In order to minimize both the torque ripple and the cogging torque, which might result in undesired effects on the EMA drive-train, 9 slots / 8 poles arrangement has been chosen [18]. Since distinguished by high fill-factor and short end-windings, a double-layer concentrated winding has been adopted, as shown in Fig. 3 [18]. This winding configuration contributes to lower copper losses, whereby the heat dissipation is facilitated. High permeability cobalt-iron alloy laminations have been used for the stator core, since they feature relatively high saturation flux density (i.e. 2.3 T) and lower specific iron losses if compared to silicon steel alloys.

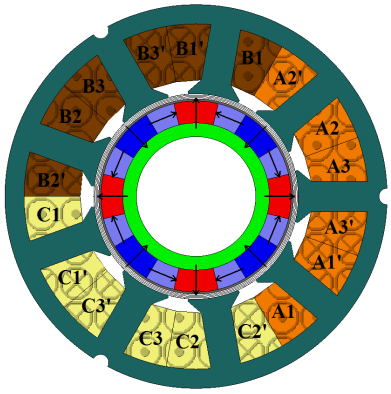

Fig. 3. Geometry and winding layout of the 9 slots / 8 poles PMSM.

In terms of permanent magnets (PMs) material, samarium-cobalt has been preferred to neodymium-iron-boron, due to the higher operating temperature capability. To increase the torque and reduce the back-electromotive force (back-EMF) harmonic content, the PMs on the rotor surface have been mounted in a quasi-Halbach array layout like highlighted by Fig. 3 [19]. Despite higher cost and manufacturing complexity, the adoption of the quasi-Halbach array configuration leads to shorter axial length, which is beneficial for both the total PMSM mass and rotor inertia. A significant efficiency improvement has been achieved by axially segmenting the PMs in 10 sectors. This approach aims at reducing the eddy current losses by shortening their paths through the PMs. Since the PMs are mechanically brittle, a titanium retaining sleeve has been used for holding the PMs on the shaft and protecting them during the PMSM assembling stage. For securing fast acceleration and containing the rotor inertia, a hollow shaft has been manufactured [20]. A magnetic permeable material (i.e. 17-4 PH stainless steel) has been selected for the shaft, in order to serve also as rotor back-iron. Finally, an aluminum housing equipped with radial fins has been designed for enhancing the heat dissipation by natural convection [21]. In Fig. 4, the main components (i.e. rotor, stator and housing) of the manufactured PMSM prototype are depicted, whereas Table I summarises its parameters.

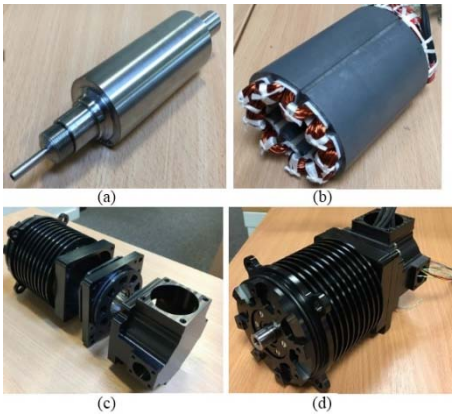

Fig. 4. PMSM prototype: (a) assembled rotor (b) wound stator core (c) housing and (d) assembled PMSM prototype.

TABLE I. PMSM Prototype Parameters

Parameter	Value
Rated Speed [rpm]	8000
Rated Torque [Nm]	5
Rated Current [A]	37.5
Phase Resistance [Ω]	0.175
d-axis Inductance [mH]	0.276
q-axis Inductance [mH]	0.274
PM Flux [Wb]	0.0225
Moment of Inertia [kg·m^2]	10^{-4}
Wire Thermal Class [°C]	180

Preliminary tests have been performed under no-load and loaded conditions on the PMSM prototype for validating the FE design. The experimental results are provided in the next sub-sections, along with the FE ones. FE analysis is also used for evaluating the PMSM performance in case of three-phase short-circuit, when the braking torque arises.

A. PMSM - No-Load Performance

Regarding the no-load PMSM performance, the flux density map and the flux lines distribution at rated speed (i.e. 8000 rpm) have been determined via FE simulations and the obtained results are presented in Fig. 5. The comparison between experimental and FE back-EMFs at rated speed is proposed in Fig. 6. In both cases, the back-EMF waveforms reveal a "perfect" sinusoidal shape (i.e. low harmonic content), proving the effectiveness of the quasi-Halbach array configuration. From Fig. 6, the slight mismatch in amplitude is observable between experimental and FE back-EMFs. This is due to the end-effect caused by the permeable rotor endcaps, which lead to an increase of leakage flux [22, 23]. The effect is not accounted in 2D FE simulations, but it is present in the real application, thus lower back-EMF is measured. Based on the FE results, the

fundamental amplitude of line-to-line back-EMF is equal to 92 V_{rms}, whereby the voltage constant is 11.5 mV_{rms}/rpm. Conversely, 86.8 V_{rms}, and 10.8 mV_{rms}/rpm are the respective values, according to the measurements (i.e. 6 % mismatch).

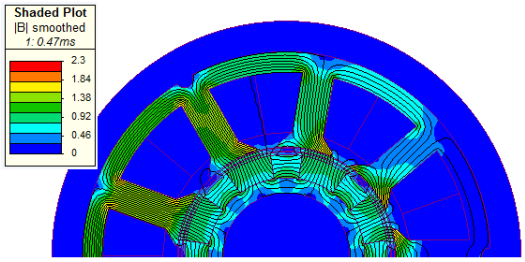

Fig. 5. No-load flux density map and flux lines distribution at 8000 rpm.

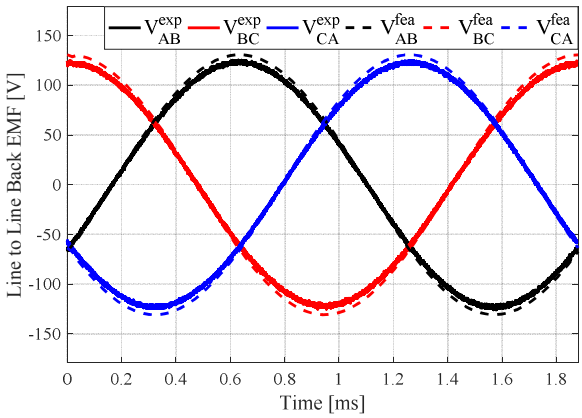

Fig. 6. Comparison between experimental (solid line) and FE (dash line) line-to-line back-EMFs at 8000 rpm.

B. *PMSM – Load Performance*

In order to develop the rated torque (i.e. 5 Nm), the PMSM must be supplied with 37.5 A (i.e. EMA active-standby operating mode).

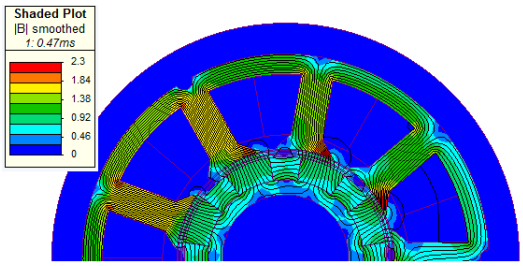

Fig. 7. Flux density map and flux lines distribution at 37.5 A and 8000 rpm.

The flux density map and the flux lines distribution at full load condition are shown in Fig. 7, while the FE instantaneous torque is depicted in Fig. 8. Looking at Fig. 7, the saturation limit (i.e. 2.3 T) is reached only in the tooth-shoe area. At the design stage, a magnetic margin has been intentionally kept, due to the possibility of feeding the PMSM with higher current for balancing the braking torque. For this reason, the flux densities in both tooth and stator yoke are fairly below 2.3 T. Indeed, in case of three-phase short-circuit, the healthy PMSM, acting on the same drive-train, should provide the double of the power (compared to the EMA active-active operating mode), while compensating the braking torque of the faulty machine (i.e. EMA active-shorted operating mode), for safely complete the EMA mission profile. From Fig. 8, 5.037 Nm average torque is generated at rated current, whereas the torque ripple results equal to 0.22 %. The PMSM torque-current characteristic has been computed by FE simulations and further experimentally validated. The comparison is shown in Fig. 9, where a good agreement between measurements and FE is highlighted. According to the FE findings, the PMSM torque constant is equal to 0.134 Nm/A, while a torque constant of 0.129 Nm/A is calculated based on experimental data (i.e. 3.7 % mismatch).

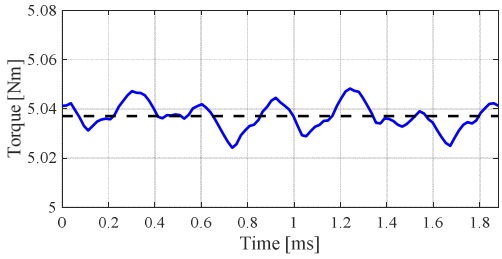

Fig. 8. Instantaneous torque at 37.5 A and 8000 rpm.

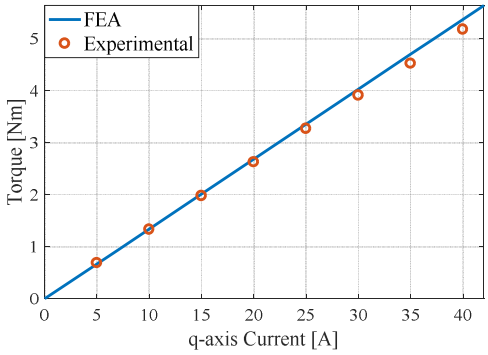

Fig. 9. Torque Vs *q*-axis current characteristic: experimental (red dots) and FE (blue solid line).

C. *PMSM – Performance During Three-Phase Short-Circuit*

A three-phase short-circuit (i.e. symmetric fault) may happen on its own or it may be intentionally induced in response to inter-turns or to phase-to-ground (i.e. asymmetric faults) fault detection [24]. By inducing a symmetric fault, the mechanical stress and the torque oscillation, caused by the asymmetric one, would be minimised. In order to quantify the braking torque, the three-phase short-circuit fault has been investigated by means of FE analysis (experimental short-circuit tests have not been performed yet at the time of writing this paper).

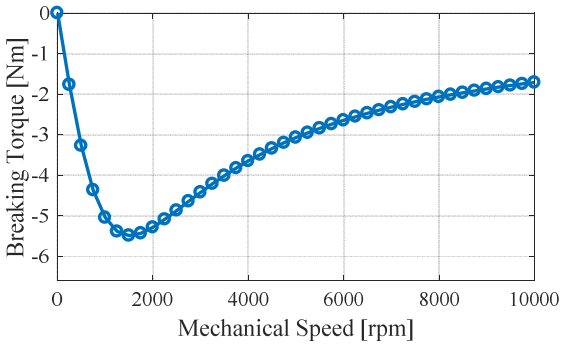

Fig. 10. Braking torque curve determined via FE simulations.

In Fig. 10, the braking torque for several rotor speeds is presented. The maximum braking torque of -5.49 Nm (109 % of

the rated torque) is detected at 1500 rpm, while at 8000 rpm, the developed braking torque is equal to -2.07 Nm (41 % of the rated torque). The latter value needs to be compensated by the healthy PMSM, in case of three-phase short-circuit at rated speed.

III. EMA Description and Performance

In safety-critical applications, redundancy is often used for increasing the system availability. Since electric drive components reveal a higher failure rate compared to the mechanical drive-train components [6], a redundant electric drive, acting on the same mechanical system, has been adopted as fault-tolerant architecture for the considered EMA (see Fig. 2). Every electric drive consists of a two-level inverter fed independently from a 270 V DC bus. Each inverter is connected to the PMSM introduced in the previous section. Conventional IGBTs and silicon diodes are used for the PECs. The linear geared EMA drive-train is characterized by two stages: 1) the gearbox, which enhances the torque produced by both PMSMs and 2) the ball screw, which converts the rotational motion of the gearbox output shaft in linear motion of the EMA rod-end. The gearbox features a 200:1 step-down ratio, while the ball screw's transmission ratio is equal to 500 rad/m. Assuming a global efficiency of 25 % for the EMA drive-train (i.e. worst-case scenario), a load force up to 125 kN can be applied to the FC surface.

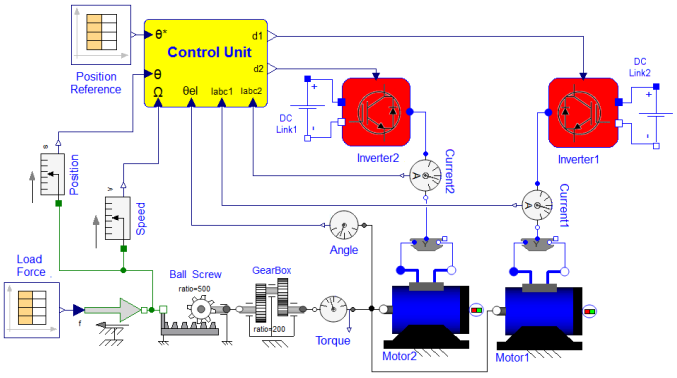

Fig. 11. EMA model in Dymola enviroment.

During a full extension, the EMA rod-end travels a stroke length of 60 mm and the extension time cannot exceed 7.5 s. Thus, the PMSM needs to accelerate from 0 to 8000 rpm in less than 0.5 s. According to its mission, the EMA performs a full extension, it holds the reached position (i.e. 60 mm) for 10 s and then it travels back in the retracted position (i.e. 0 mm), while the load force is continuously applied. The rod-end position is tracked by a cascaded control structure [25]. In particular, the inner loops control the *dq* current components of both PMSMs, while the outer loop regulates the rod-end speed. Finally, the rod-end position is supervised by the outermost loop. The system-level model of the linear EMA has been implemented in Dymola environment, as depicted in Fig. 11. For sake of drawing clarity, only one control unit is shown in Fig. 11. Nevertheless two control units are employed for ensuring redundancy also on the control side (see Fig. 2), like in the real application. Custom-made models have been used for the electric drive components [16], whereas standard Dymola blocks have been adopted for the mechanical components. The EMA performance are evaluated in active-active, active-standby and active-shorted operating modes [12], as discussed in the following sub-sections.

A. Active-Active Operating Mode

In active-active configuration, both PMSMs equally concur to the EMA mission profile. The PMSMs are supplied with half of the rated current (i.e. 18.75 A), generating 2.5 Nm each. This operating mode is desirable, due to the lower current required for counteracting the load force.

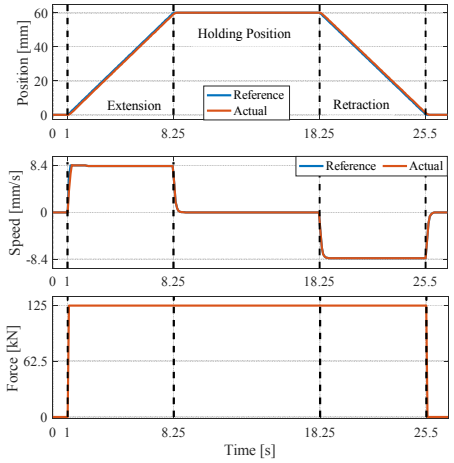

Fig. 12. EMA active-active mode: position (top sub-plot), speed (middle sub-plot), and load force (bottom sub-plot) of the EMA end-rod.

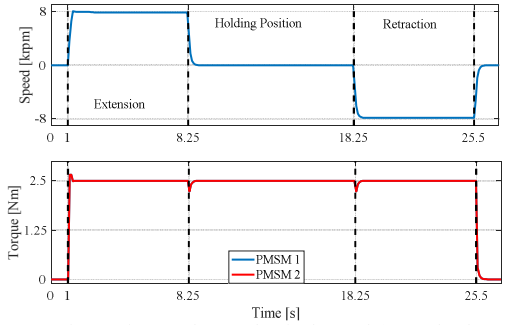

Fig. 13. EMA active-active mode: mechanical speed (top sub-plot) and torque (bottom sub-plot) of the PMSMs.

Indeed, lower current results in lower copper losses, hence easier thermal management. The simulation results for the active–active configuration are summarized in Fig. 12 and Fig. 13, where the mechanical quantities at both EMA end-rod and PMSMs' shafts are respectively shown. From Fig. 12, the EMA exhibits suitable dynamic performance, although a modest position tracking error is present during both acceleration and deceleration periods. Similarly, both PMSMs reach the rated speed in 0.3 s, complying with the acceleration time constraint.

B. Active-Standby Operating Mode

In active-standby configuration, the EMA mission profile is solely performed by one PMSM, while the other is kept as a backup. Hence, the active PMSM develops the rated torque by absorbing the rated current (i.e. 37.5 A). In this condition, the PMSM copper losses are doubled compared to the active-active configuration, thus, more heat needs to be dissipated, as highlighted in section IV. The simulation results for active–standby configuration are shown in Fig. 14 and Fig. 15. Considering the mechanical quantities at the EMA end-rod (Fig. 14), a satisfactory position tracking error is achieved along the whole trajectory; despite the saturation of the speed controller output, during the extension acceleration. This effect

is also observable on both the speed and torque of the PMSM (Fig. 15). Indeed, the acceleration from 0 to 8000 rpm is performed in 0.49 s.

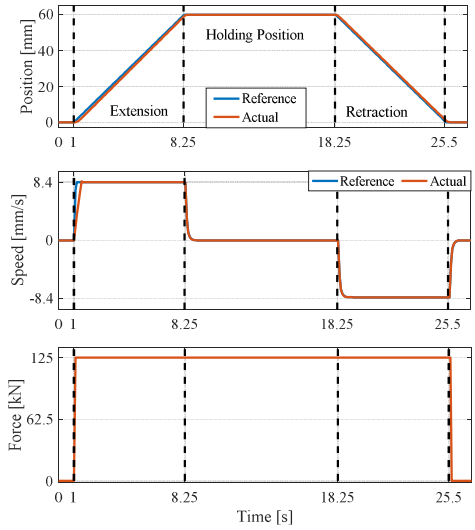

Fig. 14. EMA active-standby mode: position (top sub-plot), speed (middle sub-plot), and load force (bottom sub-plot) of the EMA end-rod.

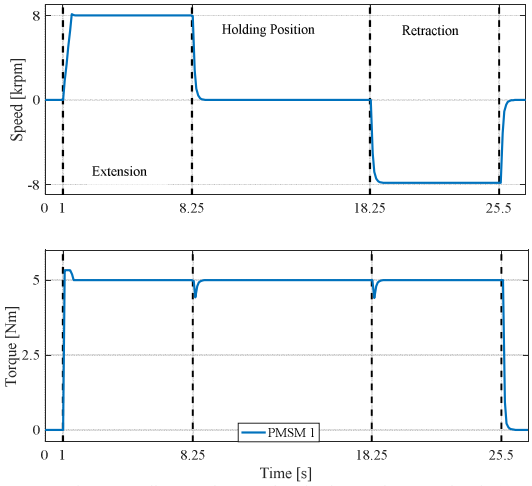

Fig. 15. EMA active-standby mode: mechanical speed (top sub-plot) and torque (bottom sub-plot) of the PMSM.

C. *Active-Shorted Operating Mode*

In active-shorted configuration, the EMA mission profile needs to be completed with one PMSM short-circuited. Therefore, the healthy PMSM must develop the rated torque, while simultaneously balancing the braking torque introduced by the short-circuited PMSM. Position, speed and torque at the EMA end-rod are reported in Fig. 16 for this operating mode. Despite significant speed oscillations, which compromise the position tracking error, the EMA is able to complete its mission profile, even under fault condition. The torque generated by both PMSMs is shown in Fig. 17, along with the shaft speed. During the extension period, the active PMSM produces 7.07 Nm (i.e. 5 Nm + 2.07 Nm), while only 5 Nm are required in the holding position period, since the braking torque is null (zero speed of the shaft). Considering the retraction stage, 2.92 Nm are developed by the healthy PMSM, because the braking torque becomes positive (i.e. +2.07 Nm), due to the speed sign change (i.e. -8000 rpm). Hence, the short-circuited PMSM "relieves the workload" of the healthy PMSM, during the retraction. For sake of completeness, the q-axis current components of both PMSMs are depicted in Fig. 18. In the most challenging condition, the active PMSM continuously requires 52.4 A (i.e. 139 % of the rated current), for completing the EMA extension. It is worth to mention that in order to safely operate the EMA the PEC must be capable of handling such a current overload.

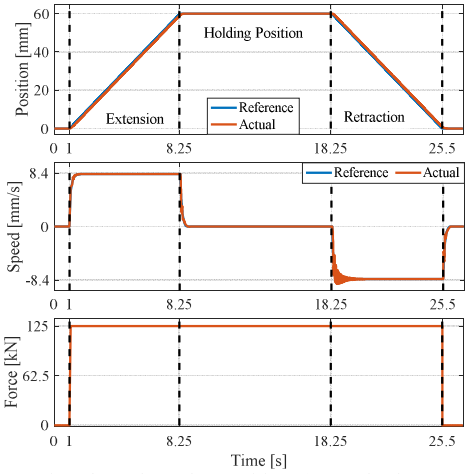

Fig. 16. EMA active-shorted mode: position (top sub-plot), speed (middle sub-plot), and load force (bottom sub-plot) of the EMA end-rod.

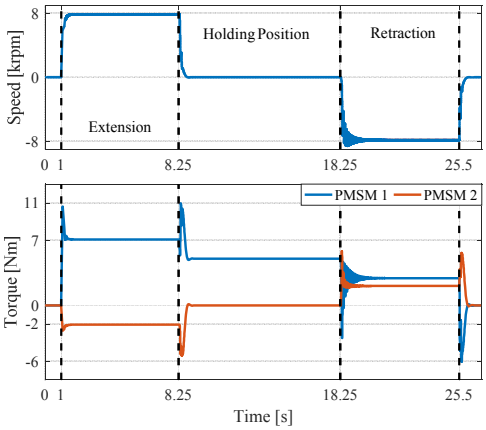

Fig. 17. EMA active-shorted mode: mechanical speed (top sub-plot) and torque (bottom sub-plot) of the PMSMs.

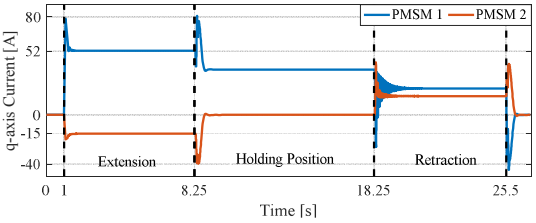

Fig. 18. EMA active-shorted mode: PMSMs' q-axis current components.

IV. Thermal Considerations

Regarding the last operating mode, the high current flowing through the healthy PMSM may create a thermal overload, which in turn may trigger critical damage and/or compromise the winding insulation lifetime [26]. Therefore, the winding temperature has been predicted and verified by using a LPTN built according to [17]. Considering adiabatic conditions (no heat is exchanged with the external ambient) and assuming a

slightly longer EMA operating time (30 s against 24.5 s), the active PMSM winding temperature profiles have been estimated in the three operating modes previously discussed. The thermal results are summarized in Fig. 19, where an initial temperature of 70 °C is assumed. The maximum temperature of 161 °C is reached when the active-shorted configuration is analysed. Since the chosen wire insulation has 180 °C thermal class, its lifetime is preserved also in the most demanding thermal condition.

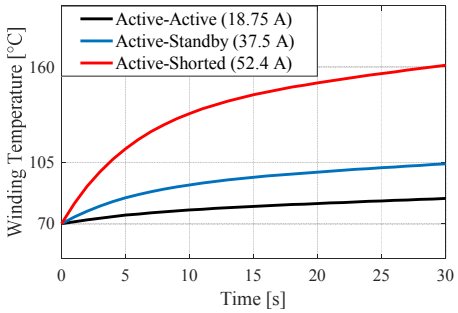

Fig. 19. Winding temperature profiles of the active PMSM during the three considered EMA operating modes.

V. Conclusions

In this paper, the design and the preliminary test results of a PMSM for aerospace EMA were presented. The PMSM performance has been evaluated via FE analysis and further compared against the experimental back-EMF waveforms and torque-current characteristic. The main outcome of the comparison is the influence of the permeable rotor endcaps, which leads to 6% and 3.7% reduction on the induced back-EMF and on the developed torque, respectively. Nevertheless, the PMSM performance is in line with the design specifications, even during the overload resulting from the EMA active-shorted operating mode. Further experimental tests are scheduled for the PMSM before moving to the EMA integration testing.

The EMA was designed for secondary FC systems and its availability was improved by adopting a redundant electric drive. The EMA behaviour was simulated in Dymola environment, considering active-active, active-standby and active-shorted operating modes. Dymola results highlighted the EMA capability of performing the required mission profile in all the simulated conditions. Finally, the winding temperature was successfully verified for each operating mode using a LPTN.

References

[1] G. Qiao, G. Liu, Z. Shi, et al., “A review of electromechanical actuators for More/All Electric aircraft systems,” in Journal of Mechanical Engineering Science, 2017.

[2] C.I. Hill, S.V. Bozhko, Y. Tao, P. Giangrande, and C. Gerada, "More Electric Aircraft Electro-Mechanical Actuator Regenerated Power Management," in 2015 *IEEE International Symposium on Industrial Electronics*, pp. 337-342, 2015.

[3] V. Madonna, P. Giangrande, and M. Galea, "Electrical Power Generation in Aircraft: review, challenges and opportunities," *in press on IEEE Transactions on Transportation Electrification,* DOI: 10.1109/TTE.2018.2834142, 2018.

[4] M. Villani, M. Tursini, G. Fabri et al., "Electromechanical actuator for helicopter rotor damper application," in 2012 International Conference on Electrical Machines.

[5] G. Altare, A. Vacca and C. Richter, "A Novel Pump Design for an Efficient and Compact Electro-Hydraulic Actuator," in 2014 IEEE Aerospace Conference.

[6] J.W. Bennett, B.C. Mecrow, D.J. Atkinson, et al., "Safety-critical design of electromechanical actuation systems in commercial aircraft," in IET Electric Power Applications, Vol. 5, Is. 1, 2011.

[7] C. Sciascera, P. Giangrande, C. Brunson, M. Galea, and C. Gerada, "Optimal design of an electro-mechanical actuator for aerospace application," in *2015 Annual Conference of the IEEE Industrial Electronics Society*, pp. 1903-1908, 2015.

[8] M. Galea, C. Gerada, T. Raminosoa, and P. Wheeler, "Design of a high force density tubular permanent magnet motor," in *Electrical Machines (ICEM), 2010, XIX International Conference on*, 2010, pp. 1-6.

[9] J.C. Derrien, “EMA advanced technologies for flight controls”, in International Congress of the Aeronautical Sciences, 2012.

[10] J. Fu, J.C. Mare and Y.L. Fu, “Modelling and simulation of flight control electromechanical actuators with special focus on model architecting, multidisciplinary effects and power flows” Chinese Journal of Aeronautic, Vol. 3, Is. 1, pp. 47-65, 2017.

[11] M.A. Ismail, E. Balaban and H. Spangenberg, “Fault Detection and Classification for Flight Control Electromechanical Actuators”, in IEEE Aerospace Conference, 2016.

[12] J.W. Bennett, B.C. Mecrow, D.J. Atkinson, et al., “Fault-tolerant electric drive for an aircraft nose wheel steering actuator”, in IET Electrical Systems in Transportation, Vol. 1, Is. 3, pp. 117-125, 2011.

[13] C. Gerada, M. Galea, and A. Kladas, "Electrical machines for aerospace applications," in IEEE Workshop on Electrical Machines Design, Control and Diagnosis, 2015.

[14] S.A. Odhano, P. Giangrande, R. Bojoi and C. Gerada, "Self-commissioning of interior permanent magnet synchronous motor drives with high-frequency current injection," in *5th IEEE Energy Conversion Congress and Exposition (ECCE),* Denver, Colorado, USA, pp. 3852-3859, 2013.

[15] S.A. Odhano, P. Giangrande, I.R. Bojoi, and C. Gerada, "Self-commissioning of interior permanent magnet synchronous motor drives with high-frequency current injection", in *IEEE Transactions on Industry Applications*, vol. 50, n. 5, pp. 3295-3303, September 2014.

[16] P. Giangrande, C.I. Hill, S.V. Bozhko, and C. Gerada, "A novel multi-level electro-mechanical actuator virtual testing and analysis tool," in *2014 IET Conference on Power Electronics, Machines and Drives*, pp. 1-6, 2014.

[17] C. Sciascera, P. Giangrande, L. Papini, C. Gerada, and M. Galea, "Analytical Thermal Model for Fast Stator Winding Temperature Prediction," in *IEEE Transactions on Industrial Electronics*, vol. 64, n. 8, pp. 6116-6126, March 2017.

[18] J. Gao, Y. Yu and S. Huang, "Winding layers and slot/pole combination in fractional slot/pole PMSM - Effects on motor performance", in International Conference on Electrical Machines and Systems, 2009.

[19] Y. Shen, “Novel Permanent Magnet Brushless Machines Having Segmented Halbach Array, PhD thesis, University of Sheffield, 2012.

[20] A. Al-Timimy, P. Giangrande, M. Degano, M. Galea, and C. Gerada, "Comparative study of permanent magnet-synchronous and permanent magnet-flux switching machines for high torque to inertia applications," in *2017 IEEE Workshop on Electrical Machines Design, Control and Diagnosis*, pp. 45-51, 2017.

[21] Z. Xu, A. Al-Timimy, M. Degano, P. Giangrande, G. Lo Calzo, H. Zhang, C. Gerada, S. Pickering, and L. Xia, "Thermal management of a permanent magnet motor for a directly coupled pump," in *2016 International Conference on Electrical Machines*, pp. 2738-2744, 2016.

[22] A. Al-Timimy, M. Alani, M. Degano, P. Giangrande, M. Galea, and C. Gerada, "Influence of Rotor Endcaps on the Electromagnetic Performance of High Speed PM Machine," in *press on IET Electric Power Applications*, 2018.

[23] P. Giangrande, F. Cupertino and G. Pellegrino, "Modelling of linear motor end-effects for saliency based sensorless control," in 2010 IEEE Energy Conversion Congress and Exposition, pp. 3261-3268, 2010.

[24] B.A. Welchko, T.M. Jahns, W.L. Soong, et al, “IPM synchronous machine drive response to symmetrical and asymmetrical short circuit faults”, *IEEE Tran. on Energy Conversion*, vol. 18, pp. 291–298, 2003.

[25] F. Cupertino, G. Pellegrino, P. Giangrande, and L. Salvatore, "Model based design of a sensorless control scheme for permanent magnet motors using signal injection," in *2010 Energy Conversion Congress and Exposition*, pp. 3139-3146, 2010.

[26] C. Sciascera, M. Galea, P. Giangrande, and C. Gerada, "Lifetime consumption and degradation analysis of the winding insulation of electrical machines," in 2016 IET Internatoional Conference on Power Electronics Machines and Drives, pp. 1-6, 2016.